Modelling and simulation of chemical looping combustion process in a double loop circulating fluidized bed reactor

Yuanwei Zhang[a,*], Zhongxi Chao[b], Hugo A. Jakobsen[a]

[a]*Department of Chemical engineering, Norwegian University of Science and Technology, Sem Sælandsvei 4, 7034 Trondheim, Norway*
[b]*Safetec Nordic AS, Klæbuveien 194, 7037 Trondheim, Norway*

Abstract

A reactive CFD model has been developed and implemented numerically in an in-house code for a coupled double loop circulation fluidized bed reactor. In the current work it is utilized for the chemical looping combustion (CLC) process but the model can easily be modified for exploring some other chemical looping processes. The air reactor and the fuel reactor are operated in fast fluidization regime and simulated separately in a simultaneous mode. The connections between the two reactors are realized through time-dependent inlet-outlet boundary conditions. The model predictions are validated by comparison with experimental data reported in the literatures. Good agreement is observed between the experiments and simulations. Using this model, fluid dynamics and chemical process performance of the double loop reactor is investigated. The results show that the methane is rapidly consumed at a very short entrance section of the reactor and the axial distribution of the oxygen is more smooth. Higher reactant residence time and fuel reactor temperature increase the conversion of methane and oxygen. The methane conversion could reach 95% during the current study.

Keywords: Chemical looping combustion; Double loop circulating fluidized bed; Interconnected multiphase reactive model;

*Corresponding author
Email address: yuanwei.zhang@ntnu.no (Yuanwei Zhang)

1. Introduction

The fact that greenhouse gas emission from the energy sector is linked to climate change has prompted research in a considerable number of technologies to address this issue. Chemical looping combustion (CLC) is one of the possible technologies which provides a novel route for inherent CO_2 capture with lower energy demand and cost penalty [1].

The typical configuration for CLC system consists of two interconnected fluidized bed reactors, comprising a fuel reactor (FR) operated as a bubbling bed and an air reactor (AR) operated in the fast fluidization regime. A metal oxide, known as oxygen carrier (OC), is used to supply the oxygen needed for fuel conversion and circulates between the two reactor units. The gaseous fuel is introduced to the FR and reacts with oxygen, provided by the OC, to give CO_2 and steam (1). In a subsequent step, this oxygen carrier is reoxidized to its initial state with air (2) in the AR. In this way, the mixing of fuel and air is avoided and CO_2 will inherently not be diluted with nitrogen which would otherwise require high energy cost. A large number of studies considering different areas of CLC have been summarized by several review papers [2–4].

$$(2n+m)\mathrm{Me_xO_y} + \mathrm{C_nH_{2m}} \rightarrow (2n+m)\mathrm{Me_xO_{y-1}} + m\mathrm{H_2O} + \mathrm{nCO_2} \quad (1)$$

$$\mathrm{MeO_{y-1}} + \frac{1}{2}\mathrm{O_2} \rightarrow \mathrm{Me_xO_y} \quad (2)$$

The development of Computational Fluid Dynamic (CFD) model for CLC process has been the focus of many researches since the mathematical modelling and simulation of the reactor is essential for its design, optimization and up-scaling. Most of CLC simulation studies available on the literature focused on modelling the typical configuration which composes of a high velocity riser as the AR and a low velocity bubbling fluidized bed as the FR[5–14], However several studies [5–8] found that the bubbles formed and the reacting gas bypassing

in the bubbling bed could result low gas conversion. Up to date, only a few attempts [15–17] were made for other reactor design possibilities.

SINTEF Energy Research and the Norwegian University of Science and Technology have designed a double loop circulating fluidized bed (DLCFB) reactor for CLC process. In the DLCFB system, the air reactor as well as the fuel reactor are operated in the fast fluidization regime for a better gas-solid contact and flexible operation. In order to understand the physical phenomena, explore the chemical process performance of the CLC process in this novel DLCFB system, it is beneficial to develop a simulation tool which further can be used to optimize the operating conditions, on scale-up and design of industrial scale reactors.

This study makes a first attempt on CFD modelling and simulations for the CLC process in the novel DLCFB reactor as defined above. A reactive multiphase CFD model for an interconnected DLCFB reactor has been developed and implemented using an in-house Fortran code. Methane is used as the gaseous fuel and NiO is chosen as OC. The main objective of this paper is to validate the model and investigate the CLC performance in the DLCFB reactor system with different operating conditions.

2. Experimental setup

The concept for the CLC reactor system developed by SINTEF Energy Research and Norwegian University of Science and Technology is schematically represented in Figure 1 (a). The air reactor as well as the fuel reactor are operated as a circulating fluidized bed (CFB) and the system is therefore called a double loop circulating fluidized bed reactor system (DLCFB). The fast fluidization regime in the FR has the objective of raising the fuel conversion with a better utilization of the upper part of the rector. The continuous solid exchange between the reactor units was realized by means of two divided loop-seals. The loop-seals are fluidized through three bubble caps (central, external and internal) so that the solids entrained by one reactor can be lead into the other reactor or re-circulated back into the original one. There is also a bottom extraction/lift

used to balancing the hold up of the two units.

Both reactors are of 6 m height while the diameter of the AR and FR is 0.23 m and 0.154 m respectively. The fluidizing gas is fed from bottom of the reactors. The solid outflow from one reactor will inject into the bottom of the other reactor through the cyclones and external loop-seals. Differential pressure transducers were placed along the reactor bodies to measure the local pressure distribution.

3. Computational model

3.1. Fluid dynamics model

A two-fluid reactive model based on the kinetic theory of granular flow (KTGF) implemented in an in-house code is used to describe the hydrodynamics and the reactions in the fluidized reactors. In the two-fluid model, each phase is described by a set of governing equations and closures. For the gas phase, the transport equations can be derived by adopting suitable averaging process for local instantaneous equations[18], while the transport equations for solid phase originate from the ensemble average of a single-particle quantity over the Boltzmann integral-differential equation[19]. Detailed descriptions of the model can be found in [20] and [21]. The governing equations are summarised in Table 1. The standard $\kappa - \varepsilon$ turbulence model is chosen for characterizing the gas phase turbulence phenomena, the corresponding closure models are shown in Tables 2 and 3. The KTGF is adopted to derive the physical properties of solid phase by introducing the granular temperature, Θ. The two phases are coupled through the interfacial momentum transfer, which is dominated by the drag force. In this study, the Gidaspow drag model [22] was used. The internal phases constitutive equations are listed in Tables 4 and 5. Table 6 summarizes the equations used for the interfacial momentum and heat transfer.

Since the reactions included in the FR are moderately endothermic and during the experiments the temperature of the FR is usually carefully controlled

within narrow range [17], thus no energy conservation was simulated in the FR. Only the AR is incorporated with the heat balance.

3.2. Reaction kinetics model

In the simulations presented in this paper, a nickel-based oxygen carrier is used. Following the experiment conducted by [17], the mean particle size and the density are 135 μm and 3416 Kg/m^3 respectively. The active NiO content is 40%. One step reactions are assumed both for the fuel and air reactors and given as follows:

$$4\mathrm{NiO} + \mathrm{CH_4} \rightarrow \mathrm{CO_2} + 2\mathrm{H_2O} + 4\mathrm{Ni} \tag{3}$$

$$4\mathrm{Ni} + 2\mathrm{O_2} \rightarrow 4\mathrm{NiO} \tag{4}$$

The reaction (3) is assumed to be first order with respect to CH_4 and the reaction rate is modeled by the expression derived by Kruggel-Emden [9]:

$$r = kS_0 \frac{\rho_g Y_{\mathrm{CH_4}}}{M_{\mathrm{CH_4}}} = kS_0 C_{\mathrm{CH_4}} \tag{5}$$

The chemical reaction rate constant k given by Ryu et al.[23] was obtained by use of a thermal gravimetrical analysis technique and expressed by:

$$k = k_0 \exp\left(-\frac{E}{RT}\right) \tag{6}$$

with the activation energy $E = 37070$ (J/mol) and the preexonential factor $k_0 = 3.27 \times 10^{-2}$ (m/s).

The S_0 represent the surface area for the reaction and is dependent on the degree of conversion X through a nonlinear relation with:

$$S_0 = \frac{6}{d_s}\alpha_s(1-X)^{2/3} \tag{7}$$

where X is the volumetric dimensionless degree of conversion, which is the ratio of the radial position of the reaction (r_c) over the external radius of the particle (r_p). It can be expressed in terms of the mass fraction Y of Ni and NiO:

$$(1-X)^{1/3} = \frac{r_c}{r_p} = \frac{Y_{\mathrm{Ni}}}{Y_{\mathrm{Ni}} + Y_{\mathrm{NiO}}(\rho_{\mathrm{Ni}}/\rho_{\mathrm{NiO}})} \tag{8}$$

The reaction rate of reaction (4) in the air reactor is given as [24]:

$$r = k_0 \alpha_s \frac{\rho_g Y_{\mathrm{O_2}}^n}{M_{\mathrm{O_2}}} \exp\left(-\frac{E}{RT}\right) [3(1-X)^{2/3}] \tag{9}$$

in which the reaction order is $n = 0.7$, the preexonential factor is $k_0 = 8.4 \times 10^{-1}$ ($\mathrm{mol}^{1-n}/\mathrm{m}^{2-3n}\mathrm{s}$) and the activation energy $E = 22000$ (J/mol).

The source term in the species mass balance equation for the jth species in the gas can be modelled by:

$$\Gamma_{g,j}^{\omega} = \nu_j M_j r \tag{10}$$

The mass transfer between the gas phase and the solid phase is calculated as following the relation proposed by Jung and Gamwo [5]:

$$\Gamma_g = \nu_{\mathrm{O_2}} M_{\mathrm{O_2}} r = -\Gamma_s \tag{11}$$

4. Interconnected reactor model and numerical considerations

4.1. Computational domain

The chemical looping combustion process is simulated by utilizing the DL-CFB system as described in Section 2. The 2D plane geometry is chosen for the simulation of the fuel and air reactors, which is shown in Figure 1 (b), having the same dimensions as the experimental setup. Grid sensitivity study was carried out in advance using three domains containing 14080, 22800 and 35250 cells in previous work by Zhang et al.[25]. In addition, the effect of the grid number on the chemical species axial distribution was also examined. The results show that the domain with 22800 cells (30×300 for FR, 46×300 for AR)

was suitable for the future studies with the consideration of the computational time and numerical accuracy.

4.2. Numerical implementation of the coupling between reactors

Two different sets of coordinates and parameters are adopted to solve the governing equations for the AR and the FR respectively. The solid flowing out of the AR is fed into the bottom of the FR, and in a similar way all the solids that exited at the outlet of FR will be injected into the bottom of the AR. The exchange of the solid flow between the reactor units is realized through the time-dependent inlet and outlet boundary conditions. At each simulation time step, the processes in the two risers are simulated separately, the solid flux of the inlet of one riser is calculated from the solid flowing out of the outlet of the other riser with the same OC condition. In the experiment, this kind of continuous solid exchange is achieved by means of cyclones, divided loop-seals and the bottom lift. The cyclones are neglected in the simulation by assuming the efficiency of the cyclones are equal to one. The bottom extraction/lift is replaced by an internal recirculation mechanism in order to keep the mass balance inside each reactor. In this way, a full loop is fulfilled for one time step. Then, another computation loop for next time step will run repeatedly.

4.3. Initial and boundary conditions

Initially, there is no gas flow in the reactor and the bed is at rest with a particle volume fraction of 0.4. A uniform plug gas flow is applied at the inlets of the reactors, the inlet solid flux of one of the reactors is kept consistent with the outlet solid flux of the other one with a prescribed solid volume fraction at the inlet. The normal velocities at all boundaries are set to zero. No-slip wall boundary condition is set for gas phase while the solids are allowed to slip along the wall, following the equation (12) from [20].

$$\vec{v}_{s,z}|_{wall} = \frac{d_s}{\alpha_s^{1/3}} \frac{\partial \vec{v}_{s,z}}{\partial r} \tag{12}$$

where $\vec{v}_{s,z}$ is the axial velocity of the particles. r indicates the radial direction.

For scalar variables but pressure, Dirichlet boundary conditions are used at the inlets, while Neumann conditions are used at the other boundaries. For the pressure correction equations, all the boundaries except outlet, Neumann conditions are adopted. At the outlet a fixed pressure is specified.

4.4. Numerical Procedure

The two-fluid model equations are discretized by finite volume method and implemented in a Fortran program. The algorithm is based on the work by Lindborg [21] and Jakobsen[20]. The second order central differential scheme is used to discretize the diffusion terms. In order to reduce the oscillation and keep higher-order accuracy of the numerical solution, a total variation diminishing (TVD) scheme is employed for discretizing the convention term [26, 27]. In this scheme, cell face values are calculated from the combination of upwind scheme part and a suitable anti-diffusive part, which controlled by a smoothness function. In this way, a higher-order discretization scheme is used in smooth regions and reduce to the first order at local extrema of the solution. The upwind part is treated fully implicitly while the anti-diffusive part is treated explicitly. The SIMPLE algorithm for multiphase flow is selected for the pressure-velocity coupling [20]. Due to the strong coupling of the two phases, the coupling terms are singled out from the discretized transport equations, and then the coupled equations are solved simultaneously by using a coupled solver. The species mass balance equations are solved by applying a fractional step scheme which decouples the chemistry (i.e., kinetics) and the transport (i.e., convection and diffusion) terms. All the linear equation systems are solved by the preconditioned Bi-conjugate gradient (BCG) algorithm [21].

5. Results and discussion

The first part of this section presents the validation of the model. Then by using the modelling tool, numerical experiments have been perform in order to explore the chemical process performance of the CLC process in the DLCFB

reactor system. The fuel feed rate for each simulation is calculated by dividing the fuel power with the lower heating value of the methane. The air flow rate to the AR could be calculated by using the air to fuel ratio.

5.1. Model validation

In order to validate the interconnected model of CLC process, the reported experimental data from Bischi et al.[28] was used. However, in their experiments, only cold flow performance was examined. In order to check the reliability of the reactive model, one more experimental CLC system documented by Pröll et al.[17] has been simulated for validating the reaction model. The detailed descriptions of the experiments can be found in [17, 28]. The simulations were run for 20 s and the results were averaged from 15 s to 20 s.

5.1.1. Validation of the coupled CFB model

The experimental facility of DLCFB in [28] is quite similar with the rig studied in current paper. Only the height of the reactor units is changing from 6 m to 5 m. During the experiment, a certain amount of the particles were present between the two reactors, so the initial inventory used in the simulations is calculated from the pressure drop between the reactor bottom and top from the experimental data.

Figure 2 shows the predicted axial profile of the pressure compare with the experimental measurement in the FR and AR respectively. The operating gas velocities of the FR and AR are 1.8 m/s and 2.1 m/s respectively. It can be seen that good agreement has been achieved for both reactors and only minor discrepancies occurred in the lower region of the reactors. One reason for the deviations may be the simplified gas distribution used at the inlet, which is not strictly consistent with the experiment. In addition, the simplified cylindrical shape of the bottom of the reactors may be another contributor to the difference.

5.1.2. Validation of the reaction model

The performance of the CLC process can be characterised by CH_4 conversion, which expressed by:

$$X_{CH_4} = 1 - \frac{\dot{n}_{CH_4,out}}{\dot{n}_{CH_4,in}} \tag{13}$$

in which $\dot{n}_{CH_4}$ is the inlet or outlet molar flow of the fuel. The optimal methane conversion is 100 % since any unburned methane must be removed before the CO_2 and H_2O separation unit. One possible method to eliminate the unburned methane is introducing pure O_2 after the CLC process, which could result in high costs.

Figure 3 shows the predicted axial profile of the pressure compared with the experimental measurement at 140 kW fuel power. The bed expansion is over-predicted by the model. This is to be expected when simulating a 3D cylindrical system on a 2D plane. The dense solids regions near to the wall will account for more in a 3D cylindrical system that they do on a 2D plane. So with the same amount of solids contained in the reactor, the bed height in 2D situation will be over-predicted [29].

Figure 4 compares the calculated and measured fuel conversion with varying fuel load. The results predicted by the reactive model are not in qualitative agreement at the lower fuel powers. This deviation might be contributed to fuel injection sources. The fuel gas is supplied through four nozzles in the experiments, which would create large bubbles in the lower regions of the reactor, hence reducing the contact between the fuel and the OC. In the simulation, however, uniform distribution is adopted for fuel supply. That could increase the contact between the gas and the solid phases and furthermore resulting the higher CH_4 conversion. Generally the predicted results seem to be in correct order, especially towards the higher fuel power.

The comparison of the computed and measured fuel conversion under different temperature conditions are illustrated in Figure 5. The CH_4 conversion is maintained at a relatively high level over all the temperatures and the pre-

dicted values are slightly lower than the measurements, indicating that the kinetic model can be used to describe the reactive behaviour of the system at the current condition.

5.2. Chemical process performance in DLCFB

The time series data for the solid mass flow are shown in Figure 6. For both reactors, the solid mass fluxes at the outlet can be seen fluctuating around a certain value after 12 s, hence the flow conditions can be said to be under quasi-steady-state. The average value of outlet solid flux in the AR (15.23 kg/s) is larger than the value in the FR (4.32 kg/s), which due to the superficial velocity in the AR is higher than in the FR.

The vertical profiles of solid volume fraction and gas concentration in both reactors are illustrated in Figure 7. The dense and dilute regions can be identified in the AR, the solids accumulate in the bottom of the reactors and decrease exponentially along the height. In the FR, the axial distribution of solid is somehow smoother. In figure 7 (b), the CH_4 is rapidly consumed at a very short entrance length and almost uniform at the upper part, the reverse trend is observed for gas products CO_2 and H_2O. The CH_4 conversion is about 91 %. In the AR, the axial distribution of oxygen concentration is relatively moderate. That is, the O_2 concentration decreases continuously along the length of the AR, thus the axial concentration profile has less gradients than the corresponding CH_4 profile.

Figure 8 shows the time-averaged radial profiles of solids volume fraction and gas concentration at different axial position above the entrance. A typical core-annulus particle distribution is established at different axial positions. Since both reactors are operating in the fast fluidization regime, similar trend can be observed in both the FR and the AR. The distribution of CH_4 and O_2, as reactants in the FR and AR, are similar. At the lower height, CH_4 or O_2 concentration appears a parabolic curve profile. The unconverted reactants in the center is higher than in the wall region, which is mainly related to the distribution of oxygen carriers. Higher concentration of oxygen carriers near the

wall enhances the reaction rate, which makes the amount of reactants lower. The distribution of reactants get flat as the height increases. The radial distribution of the products, CO_2 and H_2O, show reverse trend, with lower amount in the center and higher amount near the wall.

5.3. Effect of operating conditions

The simulation analyses under different operation conditions were conducted in this section. The fuel power and FR temperature can be varied, one at a time.

The effect of fuel power on the CH_4 concentration along the reactor height is presented in Figure 9 (a). The simulation results shows that the conversion of CH_4 decreases from 92% to 81% as the fuel power is increased from 150 kW to 250 kW. The gas velocity data presented in Figure 10 illustrates the reason for the lower performance at the higher fuel power conditions. In Figure 10, one can observe that the gas velocity increase along the axial direction, which is because more gas will be released as the reaction (3) goes on (one mole CH_4 input will gives three mole gas of CO_2 and H_2O output). The higher fuel power results in higher gas velocity and then reduce the fuel residence time as shown in Figure 11. The influence on the CH_4 conversion below the 200 kW fuel power is quite small, which shows somehow the operational flexibility for the DLCFB reactor.

The model simulations predict that higher fuel power gives lower methane conversion. It is noted that Kolbitsch [30] observed the same trend in his simulations. However, the reason of this phenomenon is different from the current study. In their study, an increased power resulted in the lower OC to CH_4 ratio which is the main reason for the lower fuel conversion. But in the current study, when the fuel power is increased, the ratio of OC to fuel is decreased a little and then increased, as shown in Figure 12. That is because with the CH_4 flow increased, the OC flow which feeds into the FR is also increased. The OC to fuel ratio (ϕ) mentioned above is defined by the following equation.

$$\phi = \frac{\dot{n}_{\mathrm{NiO,in}}}{4\dot{n}_{\mathrm{CH_4,in}}} \tag{14}$$

in which $\dot{n}_{\mathrm{NiO,in}}$ is the molar flow of NiO and $\mathrm{CH}_{4,\mathrm{in}}$ is the inlet molar flow of CH_4 in the FR. A value of $\phi = 1$ corresponds to the stoichiometric $\mathrm{NiO} - \mathrm{CH}_4$ in the reaction (3), which is also shown in Figure 12 as the optimal ratio.

The variation of the O_2 concentration along the height of the reactor is plotted in Figure 9 (b) at different fuel power conditions. In this figure, it can be seen that as the fuel power increases, the O_2 exit concentration increases. That is mainly because the higher air flow rate is needed when the power is increased in the FR in order to keep λ be 1.1, results in a shorter residential time of reactants.

Figure 13 shows the effect of varying the power on the OC temperature in the AR. The results show an increasing OC temperature along the reactor height, which is attributed to the heat being released by the exothermic reaction (4). For the cases from 150 kW to 250 kW, higher fuel power can reduce the OC temperature. That is because the amount of oxygen carriers transported from the FR, with a lower temperature, to the AR is increased.

According to Kolbitsch [30], the reaction temperature is the most important operating parameter to affect the CLC performance. In order to evaluate the influence of the temperature on the CLC performance, simulations were run varying the FR temperature. It should be emphasized that the reaction rate constant for the oxidation of Ni particles was determined for the temperature range from 1073 K to 1223 K. [24] Any operating temperatures outside this range of temperature might not be physically predicted by the current model. However three temperatures, 1100 K, 1150 K, 1200 K, were chosen to examined the influence of reaction temperature on the CLC performance.

The results from a FR temperature variation are shown in Figure 14. As expected, a higher FR temperature gives higher CH_4 and O_2 conversion, which is attributed to an increase of the reaction rate according to the equation 5 and 9. For CH_4, the conversion could be up to 95%. In general higher temperature enhances the reaction rates, but extremely high temperature may give technical problems, such as sintering of bed material. So in order to optimize the reactor performance at an appropriate temperature for the CLC process, it is important

to improve the reaction rate as well as maintain the reactivity of the oxygen carrier.

6. Conclusion

A two-fluid reactive simulation tool has been developed to predict the behaviour of the CLC process in an interconnected DLCFB and implemented numerically in Fortran. The model can easily be modified to investigate different reaction processes and other chemical looping technology. First the model is validated against the experimental data obtained from the work of Bischi et al.[28] and Pröll et al.[17]. Then the influences of operation conditions on the performance of the CLC process are analysed. The results are summarized below:

- Good agreement was observed between the predicted and the measured values, indicating the capability of the model for describing the CLC process in the novel DLCFB reactor.
- The fuel (CH_4) is rapidly consumed at a very short entrance section and the species concentration becomes almost uniform at the upper part. The axial distribution of the oxygen concentration is continuously decreasing.
- Core-annular flows exist in both reactors. The gas species concentrations in the radial direction are determined by the OC concentration.
- Due to the shorter residence time of reactants, the higher fuel power would decreased the methane conversion in the FR as well as the oxygen conversion in the AR.
- An increased temperature could increased the conversion of the fuel and the oxygen since it enhance the reaction rate.

The methane conversion could reach to 95% in the current study which shows a potential for the further research. Further work continues to optimize of operating conditions including air to fuel ratio, oxygen carrier inventory and

test the different types of oxygen carriers such as copper-based or manganese-based oxygen carriers.

Acknowledgments

This work is part of the BIGCLC project supported by the Research Council of Norway (224866) and the BIGCCS Centre, performed under the Norwegian research program Centres for Environment-friendly Energy Research (FME). The authors acknowledge the following partners for their contributions: Gassco, Shell, Statoil, TOTAL, ENGIE and the Research Council of Norway (193816/S60).

Nomenclature

Roman Symbols

Symbol	Description	Unit
C_1, C_2, C_b, C_μ	Turbulence model parameter	-
d_s	Particle diameter	m
D_{ji}	Binary diffusion coefficient	m^2/s
$D_{k,j}$	Diffusion coefficient for component j in phase k	m^2/s
E	Activation energy	J/mol
e	Coefficient of restitution	-
g_0	Radial distribution function	-
h	Heat transfer coefficient	$kW/(m^2K)$
H_i^R	Reaction enthalpy for reaction i	kJ/mol
k	Reaction rate coefficient	m/s

k_g	Gas turbulent kinetic energy	m^2/s^2
M	Mole mass	kg/kmol
p_k	Pressure of phase k	Pa
Pr	Prandtl number	-
Q	Heat transfer	J/m^3s
R	Gas constant	J/Kmol
Re	Reynolds number	-
Re_p	Particle Reynolds number	-
S_0	Surface area of the reaction	1/s
S_t	Turbulent kinetic energy production	kg/m^2s^2
T	temperature	K
t	Time	s
X	Conversion	-
Y_j	Mass fraction of j	-
z	Axial coordinate	m
$\bar{\bar{\mathrm{I}}}$	Unit tensor	-
$\vec{F}_D$	Drag force	kg/m^2s^2
$\vec{g}$	Gravity acceleration	m/s^2
$\vec{M}_k$	Interfacial momentum transfer of phase k	kg/m^2s^2
$\vec{v}_k$	Velocity of phase k	m/s

Greek Symbols

Symbol	Description	Unit
α_k	Volume fraction of phase k	-
$\bar{\bar{\tau}}_k$	Stress tensor of phase k	Pa
$\bar{\bar{\tau}}_t$	Turbulent stress tensor	Pa
β	Interfacial drag coefficient	-
Γ	Interfacial mass transfer rate	$\mathrm{kg/m^3m}$
γ_s	Collisional energy dissipation	$\mathrm{kg/m^3s}$
κ_s	Conductivity of granular temperature	kW/mK
λ_k	Thermal conductivity of phase k	kW/mK
μ_k	Viscosity of phase k	$\mathrm{Pa \cdot s}$
ν_j	Stoichiometric coefficient	-
ω	Mass fraction	-
Θ	Granular temperature	$\mathrm{m^2/s^2}$
ε_g	Turbulent energy dissipation rate	$\mathrm{m^2/s^3}$

Subscripts

Symbol	Description	Unit
AR/FR	Air reactor or fuel reactor	-
B	Bulk	-
i	Reaction number	-
k	Gas(g) or solid(s) phase	-
mf	Minimum fluidization	-

t	Turbulent	-
w	Wall	-

Superscripts

Symbol	Description	Unit
0	Initial	-
$dilute$	Dilute	-
e	Effective	-
m	Molecular	-
max	Maximum	-

References

[1] M. Ishida, H. Jin, A novel chemical-looping combustor without nox formation, Ind. Eng. Chem. Res. 35 (7) (1996) 2469–2472.

[2] H. Yang, Z. Xu, M. Fan, R. Gupta, R. B. Slimane, A. E. Bland, I. Wright, Progress in carbon dioxide separation and capture: A review, J. Environ. Sci. 20 (1) (2008) 14–27.

[3] J. Adanez, A. Abad, F. Garcia-Labiano, P. Gayan, F. Luis, Progress in chemical-looping combustion and reforming technologies, Prog. Energy Combust. Sci. 38 (2) (2012) 215–282.

[4] A. Nandy, C. Loha, S. Gu, P. Sarkar, M. K. Karmakar, P. K. Chatterjee, Present status and overview of chemical looping combustion technology, Renew. Sustainable Energy Rev. 59 (2016) 597–619.

[5] J. Jung, I. K. Gamwo, Multiphase cfd-based models for chemical looping combustion process: fuel reactor modeling, Powder Technol. 183 (3) (2008) 401–409.

[6] Z. Deng, R. Xiao, B. Jin, Q. Song, H. Huang, Multiphase cfd modeling for a chemical looping combustion process (fuel reactor), Chem. Eng. Technol. 31 (12) (2008) 1754–1766.

[7] Z. Deng, R. Xiao, B. Jin, Q. Song, Numerical simulation of chemical looping combustion process with caso 4 oxygen carrier, Int. J. Greenh. Gas Control 3 (4) (2009) 368–375.

[8] B. Jin, R. Xiao, Z. Deng, Q. Song, Computational fluid dynamics modeling of chemical looping combustion process with calcium sulphate oxygen carrier, Int. J. Chem. Reactor Eng. 7 (1) (2009) A19.

[9] H. Kruggel-Emden, F. Stepanek, A. Munjiza, A study on the role of reaction modeling in multi-phase cfd-based simulations of chemical looping combustion, Oil Gas Sci. Technol. 66 (2) (2011) 313–331.

[10] K. Mahalatkar, J. Kuhlman, E. D. Huckaby, T. O'Brien, Computational fluid dynamic simulations of chemical looping fuel reactors utilizing gaseous fuels, Chem. Eng. Sci. 66 (3) (2011) 469–479.

[11] H. Kruggel-Emden, S. Rickelt, F. Stepanek, A. Munjiza, Development and testing of an interconnected multiphase cfd-model for chemical looping combustion, Chem. Eng. Sci. 65 (16) (2010) 4732–4745.

[12] A. Bougamra, L. Huilin, Modeling of chemical looping combustion of methane using a ni-based oxygen carrier, Energy Fuels 28 (5) (2014) 3420–3429.

[13] Y. Guan, J. Chang, K. Zhang, B. Wang, Q. Sun, Three-dimensional cfd simulation of hydrodynamics in an interconnected fluidized bed for chemical looping combustion, Powder Technol. 268 (2014) 316–328.

[14] C. Geng, W. Zhong, Y. Shao, D. Chen, B. Jin, Computational study of solid circulation in chemical-looping combustion reactor model, Powder Technol. 276 (2015) 144–155.

[15] S. Wang, H. Lu, F. Zhao, G. Liu, Cfd studies of dual circulating fluidized bed reactors for chemical looping combustion processes, Chem. Eng. J. 236 (2) (2014) 121–130.

[16] M. A. Hamilton, K. J. Whitty, J. S. Lighty, Numerical simulation comparison of two reactor configurations for chemical looping combustion and chemical looping with oxygen uncoupling, J. Energy Resour. Technol. 138 (4) (2016) 042213.

[17] T. Pröll, P. Kolbitsch, J. Bolhàr-Nordenkampf, H. Hofbauer, A novel dual circulating fluidized bed system for chemical looping processes, AlChE J. 55 (12) (2009) 3255–3266.

[18] H. Enwald, E. Peirano, A. E. Almstedt, Eulerian two-phase flow theory applied to fluidization, Int. J. Multiphase Flow 22 (1996) 21–66.

[19] J. Ding, D. Gidaspow, A bubbling fluidization model using kinetic theory of granular flow, AlChE J. 36 (4) (1990) 523–538.

[20] H. A. Jakobsen, Chemical Reactor Modeling, 2nd Edition, Springer-Verlag, Multiphase Reactive Flows, Berlin, Germany: Springer-Verlag, 2014.

[21] H. Lindborg, Modeling and Simulation of Reactive Two-Phase Flows in Fluidized Bed Reactors, Ph.D. thesis, Norwegian Institute of Technology, Trondheim, Norway (2008).

[22] D. Gidaspow, Multiphase flow and fluidization: continuum and kinetic theory descriptions, Academic press, San Diego, US, 1994.

[23] H.-J. Ryu, D.-H. Bae, K.-H. Han, S.-Y. Lee, G.-T. Jin, J.-H. Choi, Oxidation and reduction characteristics of oxygen carrier particles and reaction kinetics by unreacted core model, Korean J. Chem. Eng. 18 (6) (2001) 831–837.

[24] C. Dueso, M. Ortiz, A. Abad, F. García-Labiano, F. Luis, P. Gayán, J. Adánez, Reduction and oxidation kinetics of nickel-based oxygen-carriers for chemical-looping combustion and chemical-looping reforming, Chem. Eng. J. 188 (6) (2012) 142–154.

[25] Y. Zhang, Z. Chao, H. A. Jakobsen, Modelling and simulation of hydrodynamics in double loop circulating fluidizedbed reactor for chemical looping combustion process, Powder Technol. 310 (2017) 35–45.

[26] B. van Leer, Towards the ultimate conservation difference scheme. ii. monotonicity and conservation combined in a second-order scheme, J. Comput. Phys. 14 (1974) 361–370.

[27] B. van Leer, Towards the ultimate conservative difference scheme. iv. a new approach to numerical convection, J. Comput. Phys. 23 (3) (1977) 276–299.

[28] A. Bischi, Ø. Langørgen, J.-X. Morin, J. Bakken, M. Ghorbaniyan, M. Bysveen, O. Bolland, Hydrodynamic viability of chemical looping pro-

cesses by means of cold flow model investigation, Appl. Energy 97 (2012) 201–216.

[29] S. Cloete, S. T. Johansen, S. Amini, An assessment of the ability of computational fluid dynamic models to predict reactive gas–solid flows in a fluidized bed, Powder Technol. 215 (2012) 15–25.

[30] P. Kolbitsch, T. Pröll, H. Hofbauer, Modeling of a 120kw chemical looping combustion reactor system using a ni-based oxygen carrier, Chem. Eng. Sci. 64 (1) (2009) 99–108.

[31] H. A. Jakobsen, On the modelling and simulation of bubble column reactors using a two-fluid model, Ph.D. thesis, Norwegian Institute of Technology, Trondheim, Norway (May 1993).

[32] C. Lun, S. B. Savage, D. Jeffrey, N. Chepurniy, Kinetic theories for granular flow: inelastic particles in couette flow and slightly inelastic particles in a general flowfield, J. Fluid Mech. 140 (1984) 223–256.

[33] J. Jenkins, S. Savage, A theory for the rapid flow of identical, smooth, nearly elastic, spherical particles, J. Fluid Mech. 130 (1983) 187–202.

[34] D. Ma, G. Ahmadi, An equation of state for dense rigid sphere gases, J. Chem. Phys. 84 (6) (1986) 3449–3450.

[35] R. Bauer, E. Schlunder, Effective radial thermal-conductivity of packings in gas-flow. 2. thermal-conductivity of packing fraction without gas-flow, Int. Chem. Eng. 18 (2) (1978) 189–204.

[36] W. CR, Diffusional properties of multicomponent gases, Chem. Eng. Prog. 46 (1950) 95–104.

[37] E. N. Fuller, P. D. Schettler, J. C. Giddings, New method for prediction of binary gas-phase diffusion coefficients, Ind. Eng. Chem. 58 (5) (1966) 18–27.

[38] D. Gunn, Transfer of heat or mass to particles in fixed and fluidised beds, Int. J. Heat Mass Transfer 21 (4) (1978) 467–476.

[39] R. Yusuf, A Computational Study of Surface to Bed Heat Transfer and Reactive Flows in Gas Fluidized Beds, Ph.D. thesis, Norwegian Institute of Technology, Trondheim, Norway (2010).

Table 1

Governing equations

Continuity equation for phase k $(k = g, s)$
$\frac{\partial}{\partial t}(\alpha_k \rho_k) + \nabla \cdot (\alpha_k \rho_k \vec{v}_k) = \Gamma_k$
Momentum equation for phase k $(k = g, s)$
$\frac{\partial}{\partial t}(\alpha_k \rho_k \vec{v}_k) + \nabla \cdot (\alpha_k \rho_k \vec{v}_k \vec{v}_k) = -\alpha_k \nabla p - \nabla \cdot \alpha_k \bar{\bar{\tau}}_k + \vec{M}_k + \alpha_k \rho_k \vec{g} + \Gamma_k^{\vec{v}}$
Species mass balance for phase k $(k = g, s)$
$\frac{\partial}{\partial t}(\alpha_k \rho_k \omega_{k,j}) + \nabla \cdot (\alpha_k \rho_k \vec{v}_k \omega_{k,j}) = \nabla \cdot (\alpha_k \rho_k D_{k,j}^e \nabla \omega_{k,j}) + \Gamma_{k,j}^{\omega}$
Molecular temperature equation for phase for gas phase
$\alpha_g \rho_g C_{p,g} \frac{DT_g}{Dt} = \nabla \cdot (\alpha_g \lambda_g^e \nabla T_g) + Q_{sg}$
Molecular temperature equation for phase for solid phase
$\alpha_s \rho_s C_{p,s} \frac{DT_s}{Dt} = \nabla \cdot (\alpha_s \lambda_s^e \nabla T_s) + (-\Delta H_i^R) r_i + Q_{gs}$
Gas turbulent kinetic energy equation
$\frac{\partial}{\partial t}(\alpha_g \rho_g k_g) + \nabla \cdot (\alpha_g \rho_g k_g \vec{v}_g) = \alpha_g (-\bar{\bar{\tau}}_t : \nabla \vec{v}_g + S_t) + \nabla \cdot (\alpha_g \frac{\mu_g^t}{\sigma_g} \nabla k_g) - \alpha_g \rho_g \varepsilon_g$
Gas turbulent energy dissipation rate equation
$\frac{\partial}{\partial t}(\alpha_g \rho_g \varepsilon_g) + \nabla \cdot (\alpha_g \rho_g \varepsilon_g \vec{v}_g) = \alpha_g C_1 \frac{\varepsilon_g}{k_g} (-\bar{\bar{\tau}}_t : \nabla \vec{v}_g + S_t) + \nabla \cdot (\alpha_g \frac{\mu_g^t}{\sigma_\varepsilon} \nabla \varepsilon_g) - \alpha_g \rho_g C_2 \frac{\varepsilon_g^2}{k_g}$
Granular temperature equation
$\frac{3}{2}\left[\frac{\partial}{\partial t}(\alpha_s \rho_s \Theta_s) + \nabla \cdot (\alpha_s \rho_s \Theta_i \vec{v}_s)\right] = -\bar{\bar{\tau}}_s : \nabla \vec{v}_s + \nabla \cdot (\kappa_s \nabla \Theta_s) - 3\beta \Theta_s - \gamma_s$

Table 2

Closure for turbulent model

Turbulent viscosity
$\mu_g^t = \rho_g C_\mu \frac{k_g^2}{\varepsilon_g}$
Turbulent kinetic energy production[31]
$S_t = C_b \beta (\vec{v}_s - \vec{v}_g)^2$
Turbulent stress tensor[20]
$\bar{\bar{\tau}}_t = -\frac{2}{3} \rho_g k_g \bar{\bar{\mathrm{I}}} + 2\mu_g^t \bar{\bar{S}}_g$

Table 3

Empirical parameters for the $\kappa - \varepsilon$ model [20].

C_μ	σ_0	σ_ε	C_1	C_2	C_b
0.09	1.00	1.30	1.44	1.92	0.25

Table 4

Constitutive equations for internal momentum transfer

Gas phase stress

$$\bar{\bar{\tau}}_g = 2\alpha_g \mu_g \bar{\bar{S}}_g$$

Solid phase stress

$$\bar{\bar{\tau}}_s = -(-p_s + \alpha_s \mu_{B,s} \nabla \cdot \vec{v}_s) - 2\alpha_s \mu_s \bar{\bar{S}}_s$$

Deformation rate for phase k $(k = g, s)$

$$\bar{\bar{S}}_k = \frac{1}{2}\left(\nabla \vec{v}_k + (\nabla \vec{v}_k)^T\right) - \frac{1}{3}(\nabla \cdot \vec{v}_k)\bar{\bar{\mathrm{I}}}$$

Solid phase pressure [32]

$$p_s = \alpha_s \rho_s \Theta_s [1 + 2(1-e)\alpha_s g_0]$$

solid bulk viscosity [32]

$$\mu_{B,s} = \frac{4}{3}\alpha_s \rho_s d_p g_0 (1+e)\sqrt{\frac{\Theta_s}{\pi}} + \frac{4}{5}\alpha_s \rho_s d_p g_0 (1+e)$$

Solid phase shear viscosity[22]

$$\mu_s = \frac{2\mu_s^{dilute}}{\alpha_s g_0 (1+e)}\left[1 + \frac{4}{5}\alpha_s g_0 (1+e)\right]^2 + \frac{4}{5}\alpha_s \rho_s g_0 (1+e)\sqrt{\frac{\Theta_s}{\pi}}$$

Conductivity of the granular temperature [22]

$$\kappa_s = \frac{15}{2}\frac{\mu_s^{dilute}}{(1+e)g_0}\left[1 + \frac{6}{5}\alpha_s g_0 (1+e)\right]^2 + 2\alpha_s^2 \rho_s d_p (1+e) g_0 \sqrt{\frac{\Theta_s}{\pi}}$$

Collisional energy dissipation [33]

$$\gamma_s = 3(1-e^2)\alpha_s^2 \rho_s g_0 \Theta_s \left[\frac{4}{d_p}\sqrt{\frac{\Theta_s}{\pi}} - \nabla \cdot \vec{v}_s\right]$$

Radial distribution function [34]

$$g_0 = \frac{1 + 2.5\alpha_s + 4.5904\alpha_s^2 + 4.515439\alpha_s^3}{\left[1 - (\frac{\alpha_s}{\alpha_s^{max}})^3\right]^{0.67802}}$$

Dilute viscosity [22]

$$\mu_s^{dilute} = \frac{5}{96}\rho_s d_p \sqrt{\pi \Theta_s}$$

Table 5

Constitutive equations for internal heat and mass transfer

Effective conductivity
$\lambda_k^e = \lambda_k^m + \frac{\mu_k^t}{\rho_k Pr^t}$
Molecular conductivity[35]
$\lambda_g^m = \frac{\lambda_g^0}{\alpha_g}(1-\sqrt{\alpha_s})$
$\lambda_s^m = \frac{\lambda_g^0}{\sqrt{\alpha_s}}(\phi A + (1-\phi\Lambda))$
$\Lambda = \frac{2}{1-B/A}\left[\frac{A-1}{(1-B/A)^2}\frac{B}{A}ln\frac{A}{B} - \frac{B-1}{1-B/A} - \frac{1}{2}(B+1)\right]$
where
$A = \lambda_s^0/\lambda_g^0, B = 1.25(\alpha_s/\alpha_g)^{10/9}, \phi = 7.26\times10^{-3}$
Effective diffusivity
$D_{k,j}^e = D_{k,j}^m + D_k^t$
Molecular diffusion coefficient[36] [20]
$D_{g,j}^m = \frac{1-\omega_j}{M_m \sum_{j\neq i}\frac{\omega_j}{M_j D_{ji}}}$
Binary diffusion coefficient[37]
$D_{ji} = \frac{T_0^{1.75}\sqrt{1/M_j + 1/M_i}}{101.325P\left((\sum V)_j^{1/3} + (\sum V)_i^{1/3}\right)^2}$
Turbulent diffusion coefficient[21]
$D_g^t = \frac{\mu_g^t}{\rho_g Sc^t}$
$D_s^t = \frac{d_p}{16\alpha_s}\sqrt{\pi}\Theta$

Table 6

Interfacial momentum and heat transfer equations

Interfacial force

$$\overrightarrow{M}_g = -\overrightarrow{M}_s = \beta(\vec{u}_s - \vec{u}_g)$$

Drag coefficients [22]

$$\beta = \begin{cases} 150\dfrac{\mu_g(1-\alpha_g)^2}{\alpha_g d_p^2} + 1.75(1-\alpha_g)\dfrac{\rho_g}{d_p}|\vec{u}_g - \vec{u}_s| & \alpha_g < 0.8 \\ \\ 0.75C_d\dfrac{(1-\alpha_g)\alpha_g}{d_p}\rho_g|\vec{u}_g - \vec{u}_s|\alpha_g^{-2.65} & \alpha_g > 0.8 \end{cases}$$

where

$$C_d = \begin{cases} \frac{24}{Re_p}[1 + 0.15(Re_p)^{0.687}] & Re_p \le 1000 \\ 0.44 & Re_p > 1000 \end{cases}$$

Interfacial heat transfer

$$Q_{gs} = -Q_{sg} = \frac{6\alpha_s}{d_p}h_{gs}(T_g - T_s)$$

Interfacial heat transfer coefficient[38]

$$h_{gs} = \frac{\lambda_g Nu}{d_p}$$

$$Nu = (7 - 10\alpha_g + 5\alpha_g^2)(1 + 0.7Re^{0.2}Pr^{1/3}) + (1.33 - 2.4\alpha_g + 1.2\alpha_g^2)Re^{0.7}Pr^{1/3}$$

Particle Reynolds number and Prandtl number

$$Re_p = \frac{\alpha_g d_p \rho_g |\vec{v}_s - \vec{v}_g|}{\mu_g}$$

$$Pr = \frac{\mu_g C_{p,g}}{\lambda_g}$$

Heat transfer with the wall [21, 39]

$$Q_{w,s} = h_{w,s}(T_w - T_s)$$

$$Q_{w,g} = h_{w,g}(T_w - T_g)$$

where

$$h_{w,s} = \frac{4}{d}\left(\frac{1}{h_{tube} + h_{pck}}\right)$$

$$h_{tube} = \frac{2\lambda_{tube}}{d_{in} ln(d_{out} - d_{in})} \quad h_{pck} = \left(\frac{\lambda_s^m \alpha_s \rho_s C_{p,s} \mid v_g \mid}{\pi z}\right)^{1/2}$$

$$h_{w,g} = 0.165Pr^{1/3}\left(\frac{\rho_g}{\rho_s - \rho_g}\right)^{1/3}\left(1 + 0.05(\frac{\mid v_g \mid - U_{mf}}{U_{mf}})^{-1}\right)^{-1}\frac{\kappa_g \alpha_g}{l_{lam}}$$

$$l_{lam} = (\frac{\mu_g}{\sqrt{g(\rho_s - \rho_g)}})^{2/3}$$

Table 7

Main geometric and operating parameters.

Description	Unit	Value
Reactor geometry		
AR height	m	6
AR diameter	m	0.23
FR height	m	6
FR diameter	m	0.154
Particle properties		
Mean particle size	μm	135
Particle density	kg/m^3	3416
Active NiO content	%	40
Operational condition		
Operating pressure	atm	1.0
Fuel power	kW	150 - 250
Lower heating value of fuel	MJ/kg	50
Inlet composition of FR	–	98% CH_4
Temperature in FR	K	1100 - 1200
Wall temperature in AR	K	1000
Global air-fuel ratio	–	1.1

Table 8

simulation parameters.

Description	Unit	Value
No. of control volume	–	22,800
Gas viscosity	kg m^{-1}s^{-1}	1.82×10^{-5}
Gas density	kg/m^3	1.2
Sphericity of particle	–	1
Restitution coefficient of particles	–	0.99
Initial bed height	m	0.75
Time step	s	1.0×10^{-4}

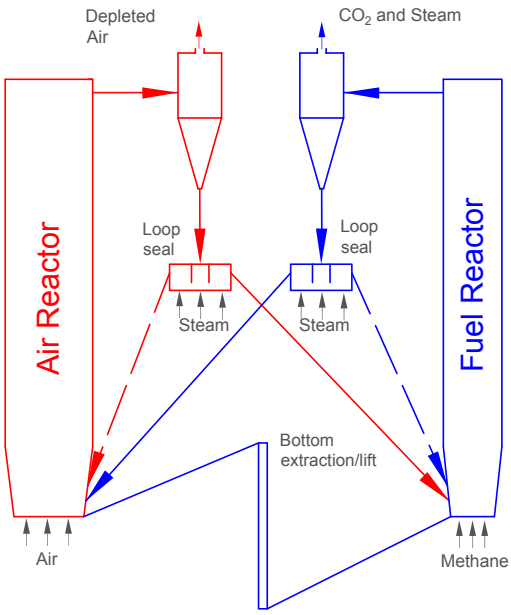

(a)

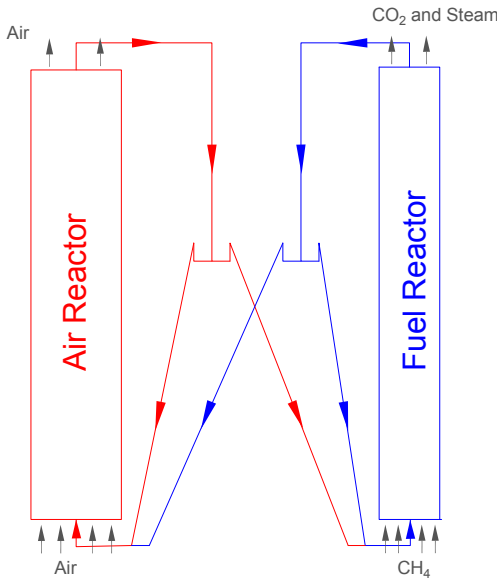

(b)

Figure 1: (a) Sketch of the double loop circulating fluidized bed reactor [28]. (b) Schematic of the 2D computational domain

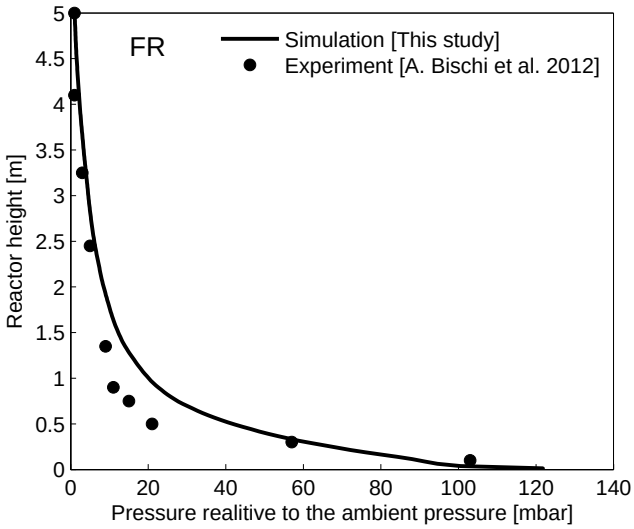

(a)

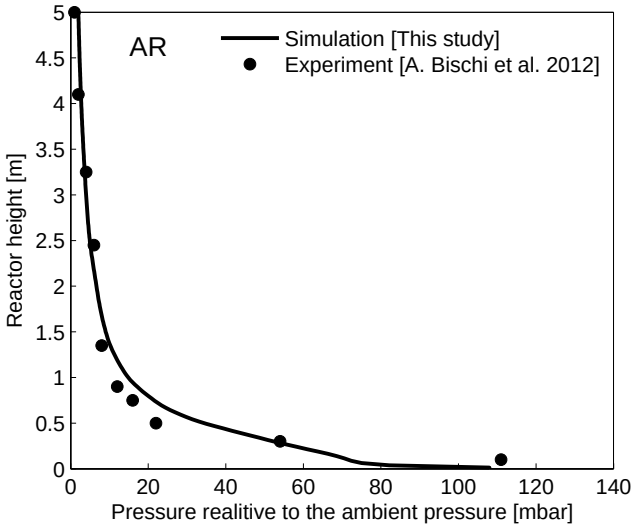

(b)

Figure 2: Comparison of pressure profiles between simulation and experimental results

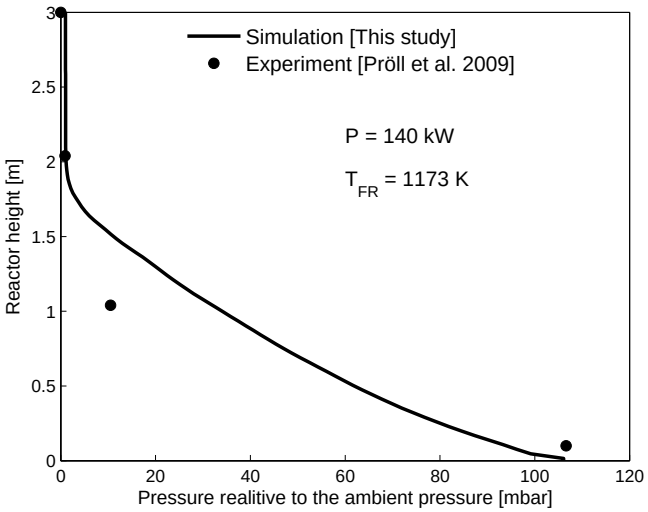

Figure 3: Comparison of pressure profiles between simulation and experimental results

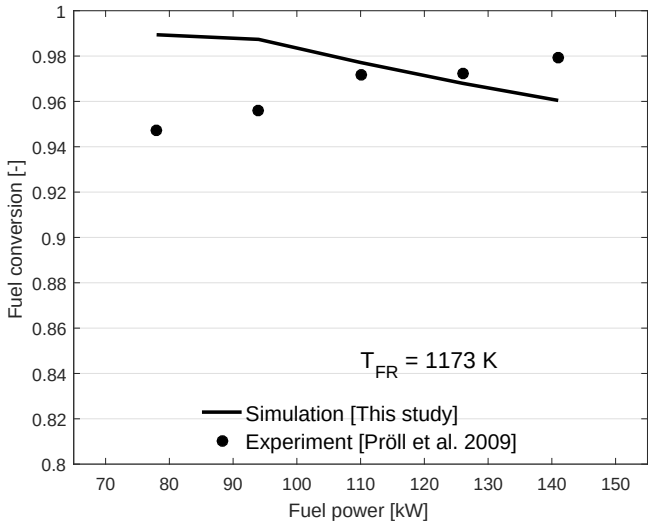

Figure 4: Comparison of fuel conversion between simulation and experimental results varying the fuel power

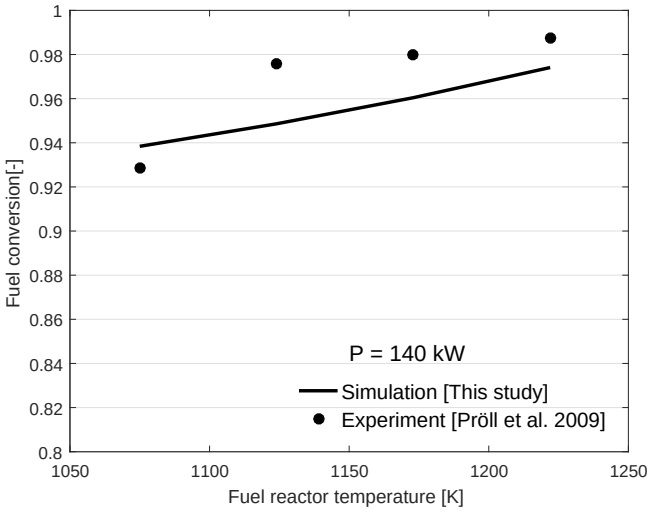

Figure 5: Comparison of fuel conversion between simulation and experimental results varying the temperature

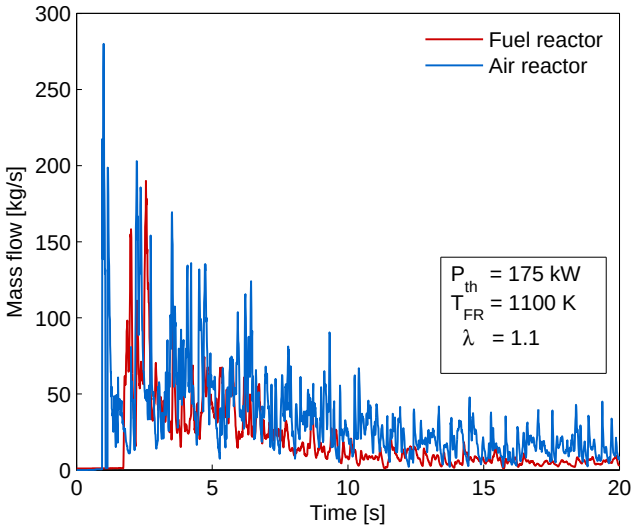

Figure 6: Solid mass flow at outlet vs. flow time

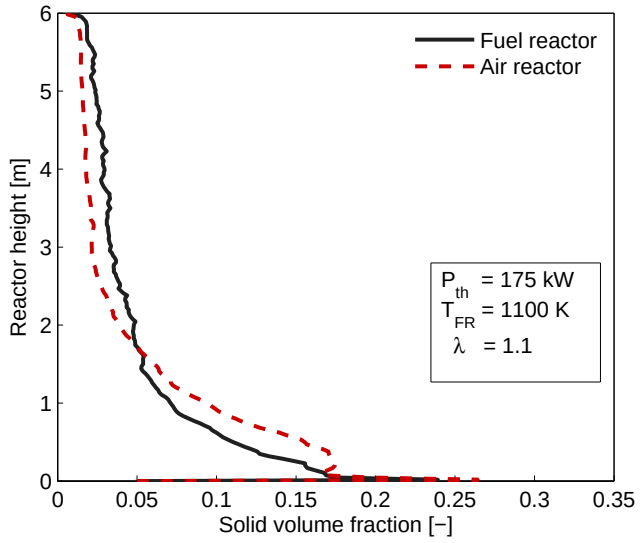

(a)

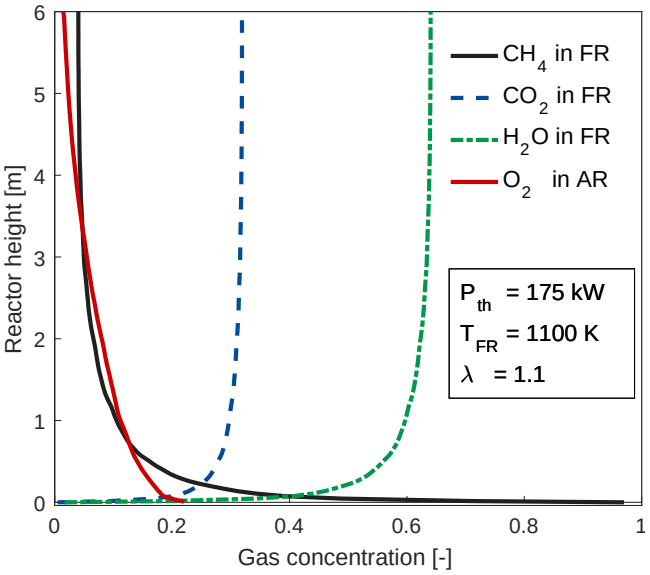

(b)

Figure 7: Axial distribution of OC (a) and gas species (b)

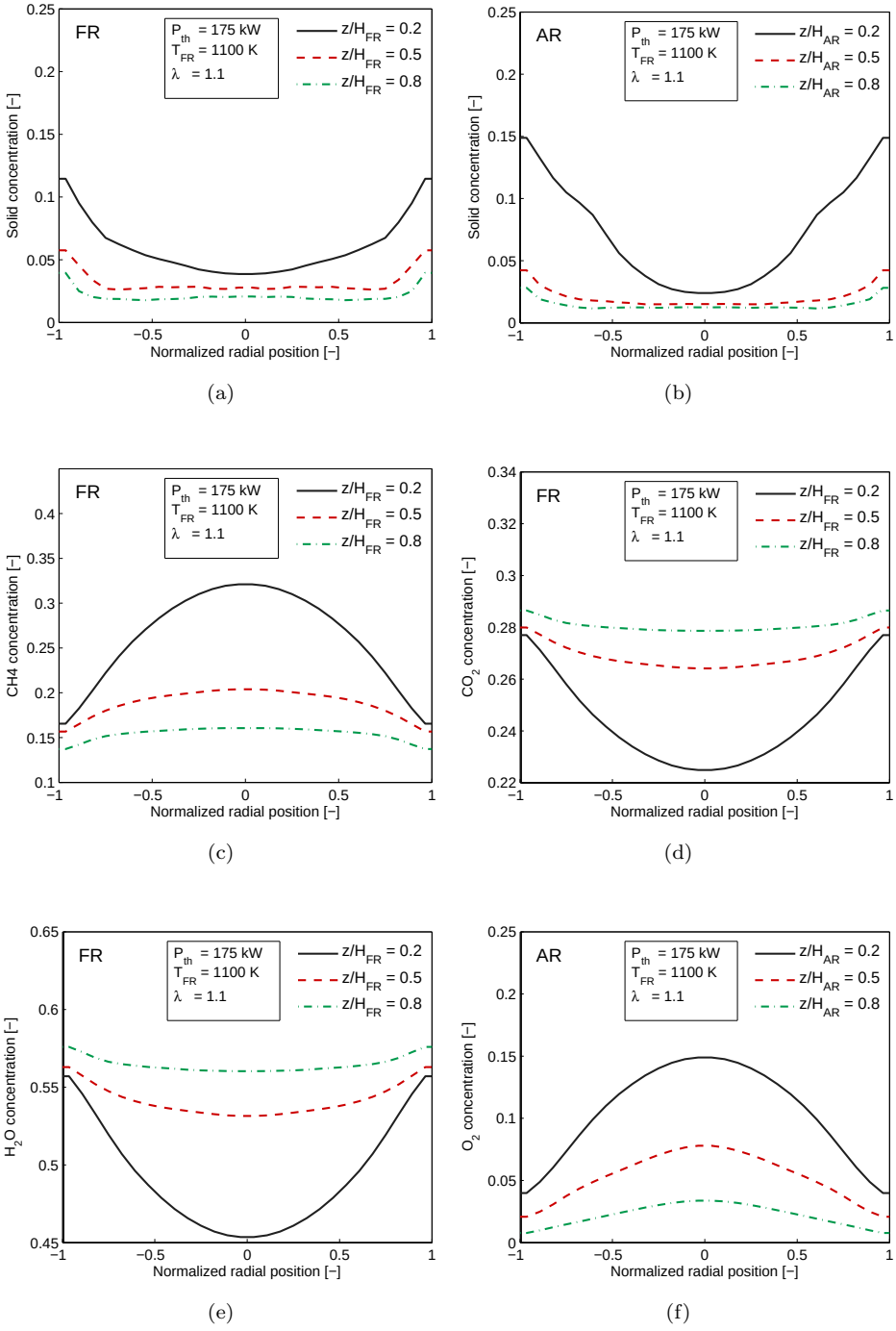

Figure 8: Radial distribution of OC and gas concentration

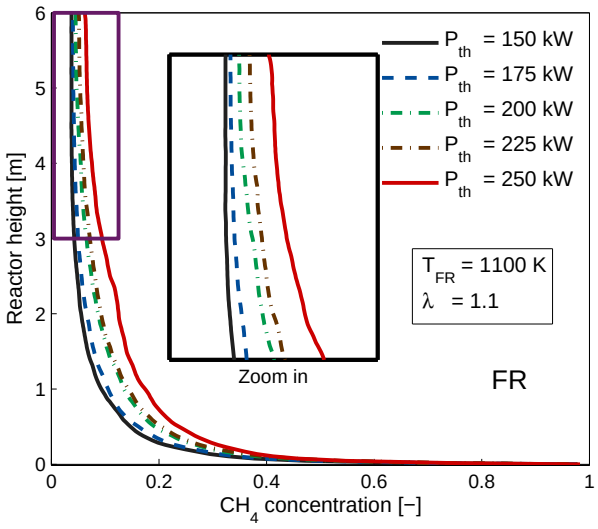

(a)

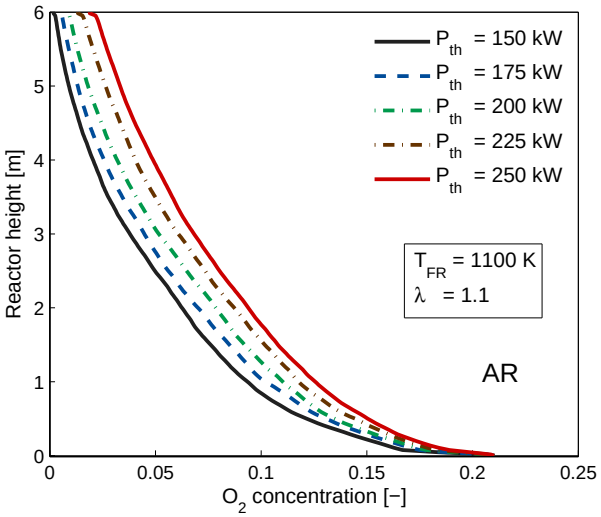

(b)

Figure 9: Axial distribution of CH_4 (a) and O_2 (b) with different fuel power

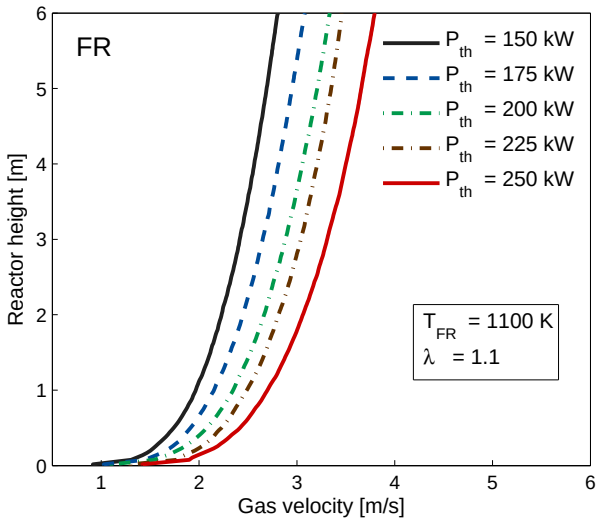

Figure 10: Axial distribution of gas velocity with different fuel power

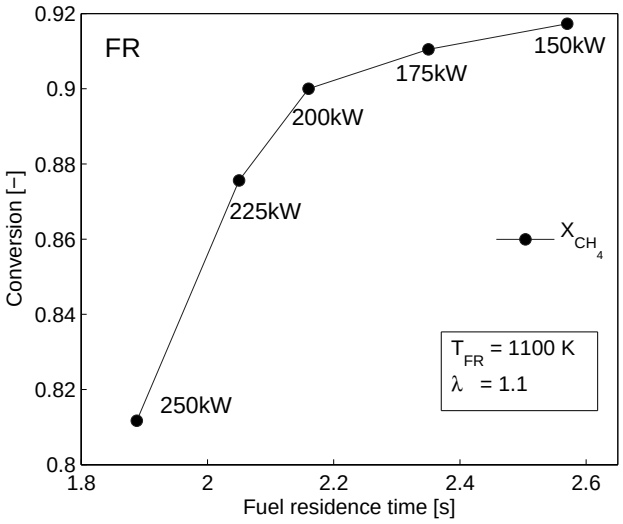

Figure 11: Gas residence time with different fuel power

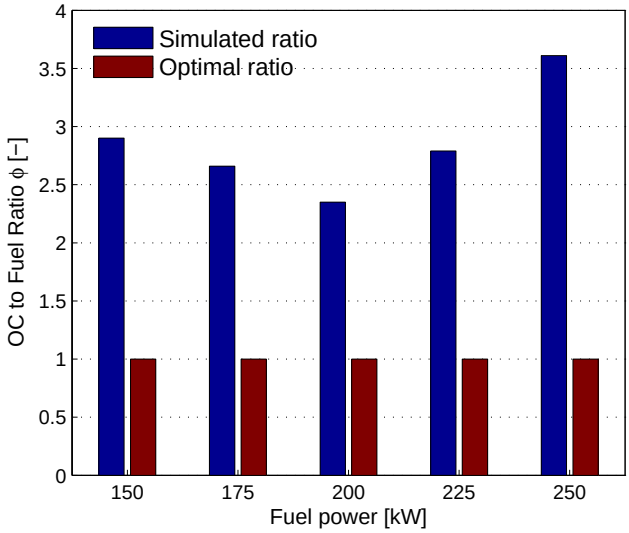

Figure 12: OC to Fuel ratio with different fuel power

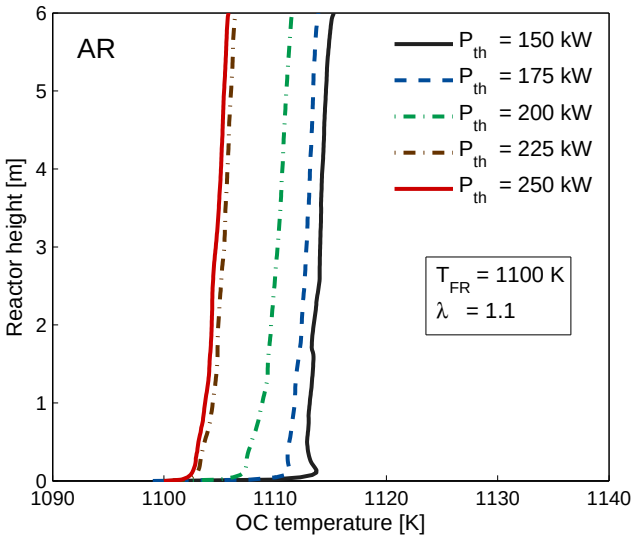

Figure 13: Axial distribution OC temperature with different fuel power

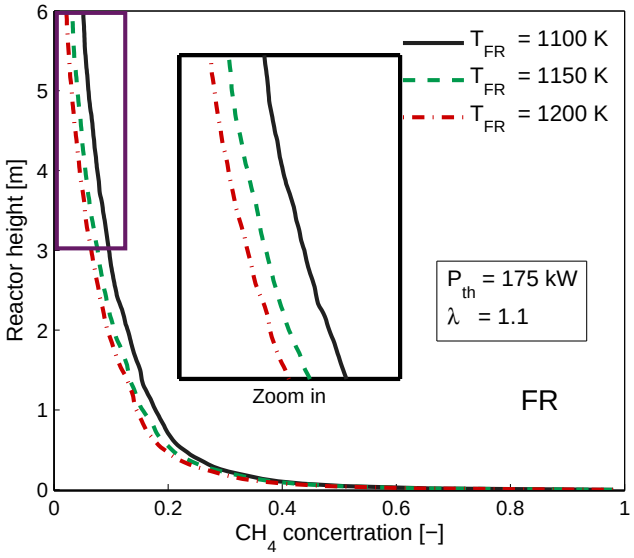

(a)

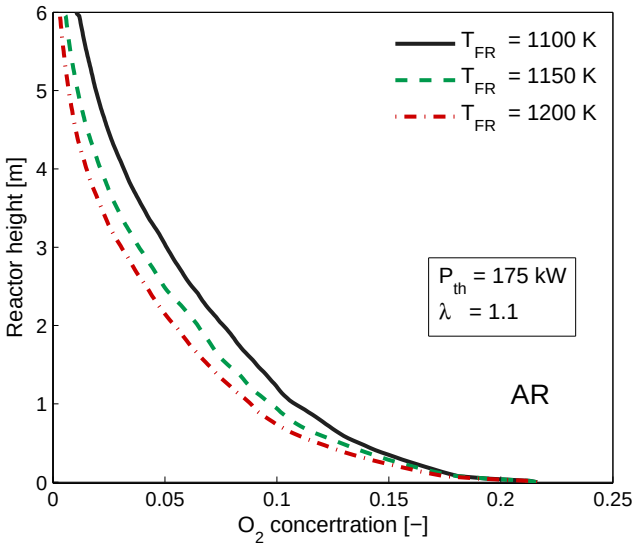

(b)

Figure 14: Axial distribution of CH_4 (a) and O_2 (b) with different FR temperature